Energy Storage Materials 35 (2021) 62–69

Contents lists available at ScienceDirect

Energy Storage Materials

journal homepage: www.elsevier.com/locate/ensm

Bulk and surface degradation in layered Ni-rich cathode for Li ions batteries: Defect proliferation via chain reaction mechanism

Chengkai Yang[a,b,c,‡,*], Ruiwen Shao[d,e,‡,*], Qian Wang[b,c,‡], Tianyi Zhou[c], Jing Lu[g], Ning Jiang[c], Peng Gao[g], Wen Liu[f], Yan Yu[a,*], Henghui Zhou[b,c,*]

[a] College of Materials Science and Engineering, Fuzhou University, 350108, Fuzhou, China
[b] College of Chemistry and Molecular Engineering, Peking University, Beijing, China
[c] China Beijing Engineering Research Center of Power Lithium-ion Battery, Beijing, China
[d] Beijing Advanced Innovation Center for Intelligent Robots and Systems and Institute of Convergence in Medicine and Engineering, Beijing Institute of Technology, Beijing 100081, China
[e] Analysis and Testing Center, Beijing Institute of Technology, Beijing 100081, China
[f] State Key Lab of Chemical Resource Engineering, College of Science & College of Energy, Beijing University of Chemical Technology, 100092, Beijing, China
[g] School of Physics, Peking University, Beijing, China

ARTICLE INFO

Keywords:
Ni-rich cathode
Lithium ion batteries
Defects
Phase transition
Defect chain reaction

ABSTRACT

Ni-rich cathode materials have emerged as a class of low-cost and high-energy-density Li ions batteries cathodes. However, the bulk and surface degradation of Ni-rich cathode remains controversial. By transmission electron microscopy (TEM), the bulk and surface degradation of nickel-rich cathode are distinguished by the causes and development time. Structure deterioration with rock-salt phase is observed in the bulk and surface region. The triggered phase transition by defect chain reaction (DCR) mechanism is unveiled by the first-principle-calculation simulations. The critical factor in DCR mechanism is the migration barrier of Ni. The decrease in migration barrier of Ni due to the oxygen vacancy and the lowering of the system energy by the Li ion compensation causes extra cation mixing and lattice distortion. Hence, Ni ion migration introduces strain perpendicular to the Ni layers with oxygen defects and Li vacancies, which leads to dislocations and defects with lattice distortion. Based on the model, a manganese oxide coating method was proposed to adjust the valence state of nickel and avoid the oxygen defects. The treated cathode presented an excellent long-term cycling performance, about 80.6% of the initial capacity after 200 cycles.

1. Introduction

Lithium ion batteries (LIB) have attracted much research interest for large-scale applications, such as electric vehicles (EV) and 3C products. The layered lithium transition metal oxides ($LiCo_xNi_yMn_{1-x-y}O_2$, $LiCoO_2$) have been studied as cathode materials to promote stability and capacity for LIB [1–4]. To meet the energy density requirement, increasing the Ni fraction li layered oxides has been adopted as a main strategy for promoting the discharge capacity [3,5]. Thus $LiNiO_2$ and Ni-rich layered oxides ($LiNi_xCo_yMn_{1-x-y}O_2$ or $LiNi_xCo_yAl_{1-x-y}O_2$, $0.8 \leq x \leq 0.95$) are potential cathode materials because of its low-cost and high capacity density (~200 mAh g^{-1}) compared with $LiCoO_2$ (~150 mAh g^{-1}). [5,6], Increasing Ni fraction will aggravate the degradation of the cathodes from R-3 m to Fm-3 m space group, verified by many previous studies [7–9]. For low nickel cathodes ($LiNi_xCo_yMn_{1-x-y}O_2$, $x \leq 0.5$), the degradation mechanism is the phase transition at the surface area, exacerbated by cation mixing with charging and discharging [10]. However, for Ni-rich cathodes the degradation mechanism is more than the surface reaction [4,9,11-13]. The capacity fading mechanism of Ni-rich cathodes ($LiNi_xCo_yMn_{1-x-y}O_2$, $x \geq 0.8$) is still controversial [14,15].

The chemical property of perfect $LiNiO_2$ crystal is unstable, which is the reason for the defects, even for Ni-rich oxide when the content of Ni is higher than 80% in total transition metal. Cation mixing of Ni, Li ions and oxygen vacancy could make the material to be non-stoichiometric $(Li_xNi_{1-x})(Ni_yLi_{1-y})O_{1-z}$. When Ni is at a high oxide state (+3 and +4), the layered oxides is a metastable phase with a trend of decomposition [8,16,17]. The oxygen evolution form the crystal structure and reduction of Ni valence state will be of frequent occurrence [18]. The existing degradation will be magnified by strain with the migration of Li. The above phenomenon provides an idea for the classification of the degradations by the causes and development time [12]. The oxygen defect decreases the migration barrier of cation mixing leading to the aggra-

* Corresponding authors.
E-mail addresses: 1058360340@qq.com (C. Yang), rwshao@bit.edu.cn (R. Shao), yuyan@fzu.edu.cn (Y. Yu), hhzhou@pku.edu.cn (H. Zhou).
‡ These authors contributed equally to this work.

https://doi.org/10.1016/j.ensm.2020.11.016
Received 1 October 2020; Received in revised form 4 November 2020; Accepted 9 November 2020
Available online 11 November 2020

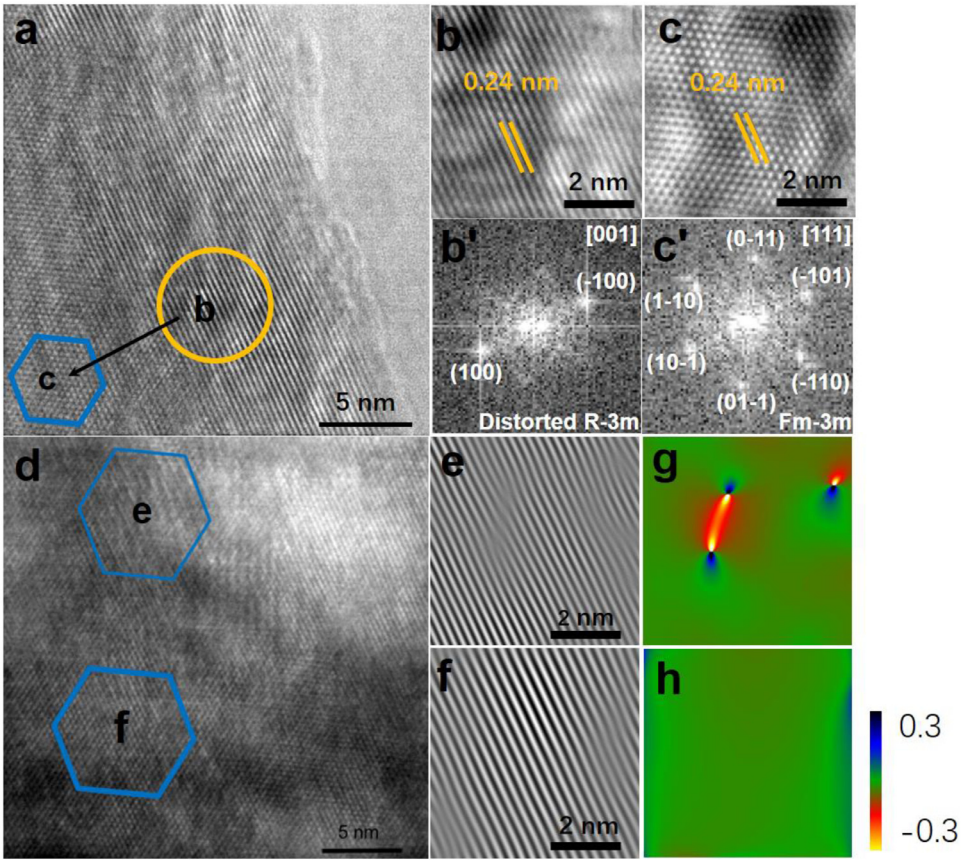

Fig. 1. The TEM characterization of intrinsic degradation in B-NCM88. (a) surface region of B-NCM88; (b-c) HRTEM images of corresponding region; (b'- c') FFT images for b and c; (d) bulk region of B-NCM88; (e-f) the FFT filtered image of corresponding region; (g-h) the GPA in-plane strain (ε_{xx}) images for e and f.

vation of rock-salt domain in J. Zheng and T. Maiyalagan's researches [1,19]. The migration of Ni ion causes lattice failure between layers which brings about the formation of dislocation observed easily by TEM by F. Lin, et. [20] There would be a link between the oxygen defect and dislocation by the migration of Ni ion in the charged state and the similar mechanism was discussed by Yongseon Kim, et. [21,22] However, a complete process of the cycling-induced degradation is still not solved well in consideration of models and thermodynamic stability. And the degradations are not classified quite well yet. Therefore, understanding the structure characteristic and evolution enables the ability to design the electrode materials in Lithium ions batteries [23].

To understand and overcome these issues, we employed the ion-beam thinning and transmission electron microscope (TEM) to analyze the slices of Ni-rich particles in combination with electrochemical measurements [24]. Analyzing technology was based on the Fast Fourier Transform (FFT), and geometric phase analysis (GPA) to deal with the crystal structure and stress-strain distribution [25]. Intrinsic degradation and cycling-induced degradation were distinguished by the causes and development time. A defect chain reaction (DCR) is proposed to explain the phase transition by the defect expansion on the results of TEM and first principle calculation. Furthermore, a micro-coated method was employed to overcome the degradation of structure and improve the cycling stability.

2. Result and discussion

2.1. Intrinsic degradation and cycling-induced degradation by TEM analysis

Intrinsic degradation are caused by the thermal motion of atoms (or ions) during solid phase reaction in the crystal, and these defects also are called as thermal defects [9]. The TEM specimens were prepared by focused ion beam (FIB) and thinning technique. Fig. 1a and 1d showed high-resolution transmission electron microscopy (HRTEM) images of a bare $LiNi_{0.88}Co_{0.08}Mn_{0.04}O_2$ (B-NCM88) primary particle. The evidence of the rock-salt phase with Fm-3 m space group from surface to bulk without cycling is shown in high magnification images (Fig. 1c, e and f), which implied the structure instability in Ni-rich layered oxides. The TEM images described the situation that was unlike in the former experiences from which the rock-salt phase existed in the surface after cycling. As shown in Fig. 1b and 1b', the FFT and its corresponding FFT filtered image of the selected region confirmed that the B-NCM88 in the region b had distorted layered structure in the surface which was prone to phase transition. In the region c (Fig. 1c and 1c'), a subsurface region, it had a Fm-3 m rock-salt structure. Similar conditions were to be found in bulk in Fig. 1d. The lattice distortion accompanied by strain field was photographed in the blue area, zoomed in Fig. 1e. Combination with an in-plane strain (ε_{xx}) image by GPA in the Fig. 1g, there was a dislocations and defects with lattice distortion. in the rock-salt domains, which was marked as a strain of tension and compression by an incomplete phase transition. The strain field in B-NCM88 was originated from the cation mixing during solid phase reaction. By contrast, the distribution of strain field in the stable transformed phase was more uniform observed in bare primary particles as shown in Fig. 1h, which suggested complete phase transition in f region. The defects above could be classed as the intrinsic defects and the generation of intrinsic defects is due to the misalignment of atoms during solid phase process based on the nature of Ni-rich materials.

Unlike the intrinsic degradation above, the cycling-induced degradation was aggravated by charge/discharge [26]. Fig. 2a was an overall view of a 200 cycle B-NCM88 particle. The B-NCM88 cathode foils were dissembled from half cells. Fig. 2e was a TEM view of a 200 cycle B-NCM88 particle showing the extensive defect structure in the surface region. Fig. 2f-h is a zoomed-in TEM view, the corresponding FFT fil-

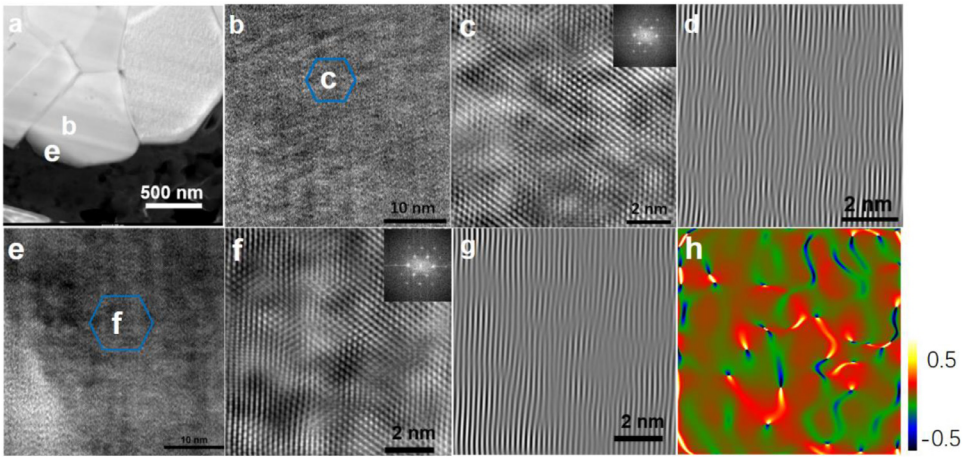

Fig. 2. The TEM characterization of cycling-induced degradation in B-NCM88 after 200 cycles. (a)The region of B-NCM88 after 200 cycles; (b) bulk region of B-NCM88; (c) HRTEM images of corresponding region; (d) the FFT filtered image for c; (e) surface region of B-NCM88; (f) HRTEM images of corresponding region; (g) the FFT filtered image for f; (h) the GPA in-plane strain (ε_{xx}) images for f.

tered image of the selected region by the (h 0 -h) frequencies and GPA images of the blue region f in Fig. 2e. The inset in Fig. 2f is an image of FFT of the corresponding region. The rock-salt structure was confirmed by lattice and FFT. The structure in the entire surface and subsurface suffered a serious deterioration. The NiO-like rock-salt phase derived from electrolyte side reaction and lattice defects dramatically increased with cycling compared with the image of the primary B-NCM88 particle [13]. The dislocations and defects with lattice distortion. increased confirmed by Fig. 2g-h. The disordered lattice could be seen as a trace of the atom migration. The distribution of dislocations and defects with lattice distortion indicated the opposite sign dislocations attracted each other. And the edge dislocations increased after cycling. The scene in Fig. 2b went in about 200 nm from the surface to bulk phase compared with it in Fig. 2e. However, it is quite rare the bulk phase would suffer from phase transition as same as the surface. The phase transition and crystal defects were revealed by the FFT filtered image in Fig. 2d. The images in surface and bulk meant badly disordered regions. So the structure evolution was not limited to the surface, which implied a new mechanism for the defect and phase transition.

2.2. First principle calculations for the DCR mechanism

To further verify the evolution of cathode, first principle calculations was adopted. A $Li_{26}Ni_{27}O_{53}$ with oxygen vacancy and a $Li_{26}Ni_{27}O_{54}$ models with R-3 m space group were established to explore the influence of oxygen vacancy in migration of Ni. The Ni ion migrates from 3a site to the adjoining 3b site (a Li vacancy), across the oxygen layer. It's easy to draw a judgment that the system reaches the saddle point when the Ni ion is at the oxygen layer without oxygen vacancy. The top view and side view for the Ni migration path without and with oxygen vacancy are shown in Fig. 3a-b. Unanimously, the calculation results in Fig. 3c shows that the migration barrier is 1.83 eV without oxygen vacancy. The energy curve reflects the oxygen layer's obstacle to the migration of Ni. However, the energy difference decreases and it is 1.31 eV when Ni at the oxygen layer with oxygen vacancy. The saddle point shifts backward and the migration barrier is 1.59 eV. Evidently, the migration barrier is dropped due to the oxygen vacancy. It is found that Ni-O bands are longer with oxygen vacancy in Fig. S3 (Supplementary Materials). The decrease in energy originates form comfortable space environments. Although the results of the saddle point make sense, the results of product are not satisfactory due to the non-spontaneous energy in thermodynamics (0.74 eV and 1.08 eV). The reason for this is that the Ni vacancy occurs in Ni layer framework after the Ni ion migration. For further verification, the two step migration path with Li ion compensations is simulated within a $Li_{26}Ni_{27}O_{52}$ model to compensate the vacancy in Ni layers in Fig. 3d. In this path, the Li ion migrates to Ni site after the migration of Ni ion, leading to an extra cation mixing. And the migration barrier for Li ion (1.09 eV) is lower than that for Ni ion (1.39 eV). More importantly, the energy of product is dropped off (−0.13 eV), which implies the stability of the structure. As a result, the two step migration lowers the energy of system and disorders the layer atoms. Based on the above analysis and experiment data, a defect chain reaction (DCR) is proposed in Fig. 3e. When the Ni ion migrates to Li site, the vertical migration-driven strain makes a disturbance to layer structure. Multiple charge/discharge cycles exacerbate the lattice distortion, leading to the dislocations and defects with lattice distortion. and phase transition. In the same way with the surface region, the Ni ion in the bulk migrated to Li sites to reduce its valence state, which was accelerated by neighboring oxygen vacancy for the lower migration barrier. In consideration of that the lattice distortion was associated with the migration of Ni ion and formation of oxygen defects, the structural instability of the bulk in B-NCM88 were explained. Ni ion migration could introduce vertical strain with oxygen defects and Li vacancies. The vertical strain introduced dislocations. Dislocations diffused with Li ion compensations to introduce new defects. Finally, the defect chain reaction occurred, which promoted the phase transition. The cation migration and oxygen defects promoted each other which causes the cathode degradation.

2.3. Mn coating method to improve structure stability

Obviously, the Li vacancy was introduced during charge and discharge, which was almost impossible to avoided. Hence, equilibrium valence state in transition metal to suppress the formation of O vacancy was regarded as the first choice. To suppress the formation of unstable Ni^{4+} species and avoid the cycling-induced defect in the charged state and surface side reaction, a Mn (oxides) coating method was employed. We modified the surface of B-NCM88 agglomerates by forming a stable layer of Mn-rich structure as interstitial coating (called as M-NCM88). The HRTEM images of M-NCM88 was shown in Fig. 4a. The distribution of Mn was uniform throughout the whole surface of particles by energy dispersive spectrometer (EDS) mapping in Fig. 4c, implying the perfect coating layer on the aggregate. As shown in Fig. 4a, the lattice of coating layer matched with internal Ni-rich layered structure and released stress concentration to avoid the damage by lithium migration. And the Mn^{4+} and Ni^{3+} have the similar ion radius (Mn^{4+}: 0.54 nm, Ni^{3+}: 0.60 nm), which the transition metal could permeated with the other in the near surface. The Mn oxides in surface diffusion layer protects the bulk material by its micro gradient. As Rietveld refinement results in Figure S1and S2 reported, the unit cell volume was extended at a degree of 0.4% after coating implying a small restructuring. Chemical state of Ni was explored by X-ray photoelectron spectroscopy (XPS) in Fig. 5a, b for M-NCM88 and B-NCM88, respectively. The binding energy of Ni^{3+} $2p_{3/2}$, Ni^{2+} $2p_{3/2}$ of the B-NCM88 sample at 855.6 eV, 854.6 eV are similar with the references reported for Ni in $LiMO_2$ (M

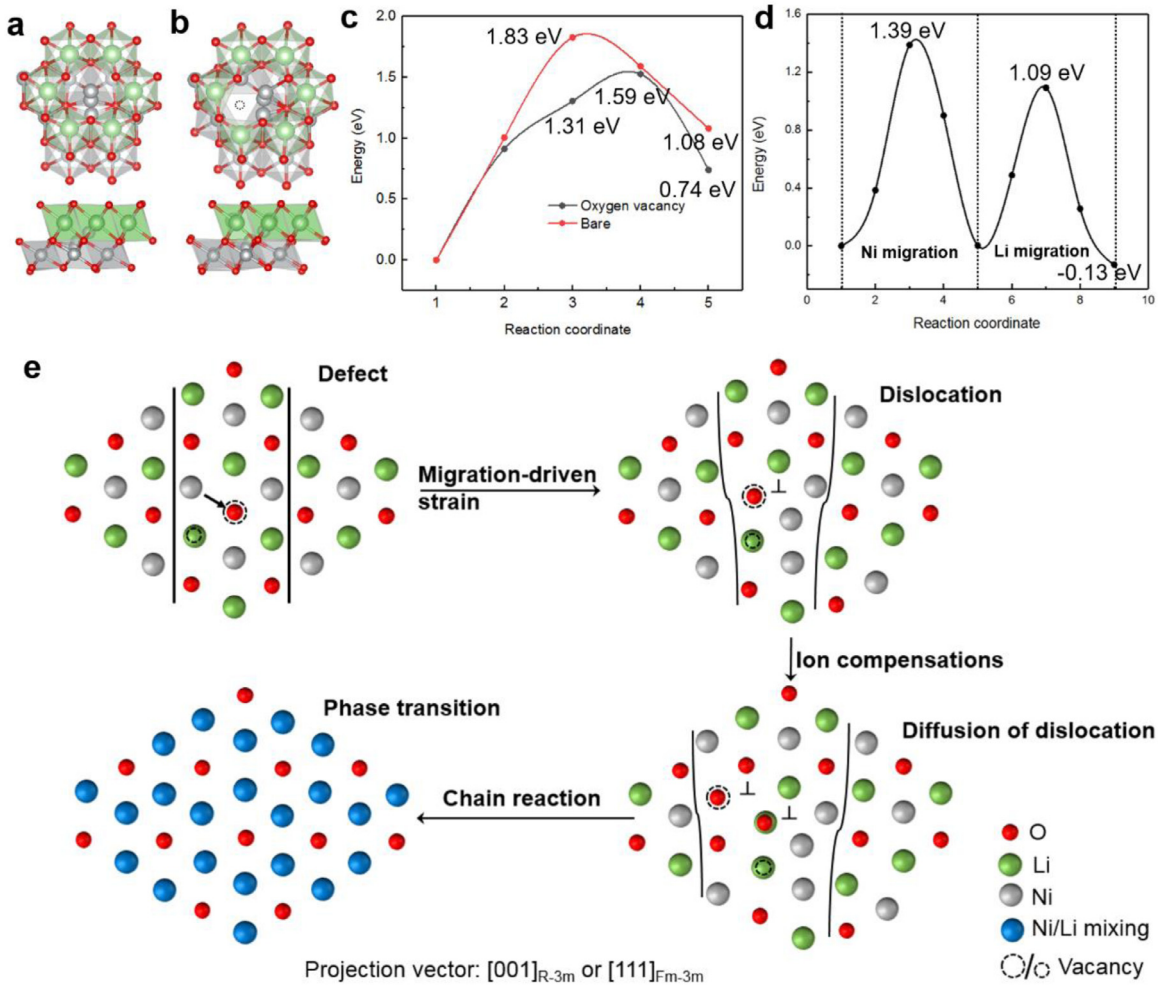

Fig. 3. First principles calculation study and evolution schematic form defects to the phase transition. (a) the top view (by c axis) and side view (by a axis) for the Ni migration path of the bare $Li_{26}Ni_{27}O_{54}$ model; (b) the top view and side view for the Ni migration path of the $Li_{26}Ni_{27}O_{53}$ model with oxygen vacancy; (c) migration barriers of two path above; (d) migration barriers with lithium ion compensations; (e) the evolution schematic of the defect chain reaction.

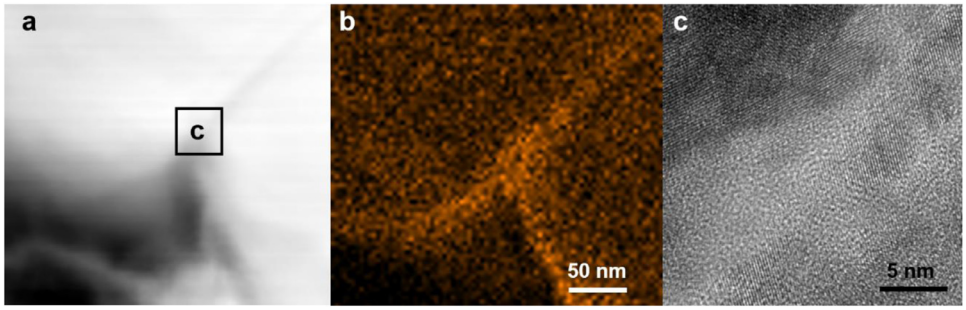

Fig. 4. (a) the EDS spectra of M-NCM88. (b) EDS spectra of Mn. (c) HRTEM images of selection area.

represents transition metals). Compared with B-NCM88 materials, there was a 0.3 eV red shift for binding energy of Ni $2p_{3/2}$ after the coating process, which suggested the reduction of Ni ion. The ratio of Ni^{3+} $2p_{3/2}$ to Ni^{2+} $2p_{3/2}$ for B-NCM88 and M-NCM88 were 9.49 and 2.46, respectively. The valence states of Ni ion were 2.904 in B-NCM88 and 2.711 in M-NCM88. It indicated that the content of Ni^{2+} at the surface region rose after coating. The analysis of XPS-peak-differenating was coincident with the chemical shift. The oxygen content from surface to bulk was characterized by XPS line scanning after cycling in Fig. 5d and the corresponding scanned region was shown in Fig. 5c. The oxygen content of M-NCM88 was higher than it of B-NCM88. The oxygen content decreased in the phase transition region. The Li intercalation/deintercalation led to stress-stain damage in the crystal structure and lattice defect, which caused oxygen vacancy in cathodes. So the structure stability was improved in M-NCM88 cathode via the Mn coating.

2.4. Electrochemistry performance

Fig. 6a was a TEM view of a 200 cycle M-NCM88 particle. The M-NCM88 cathode foils were dissembled from half cells under the same condition with B-NCM88. The Fig. 6a-d showed slice of M-NCM88 particle in bulk of the R-3 m space group. Compared with B-NCM88, M-NCM88 cathodes had a stable structure with less rock-salt domain. And the strain distribution was more uniform in Fig. 6e implying the

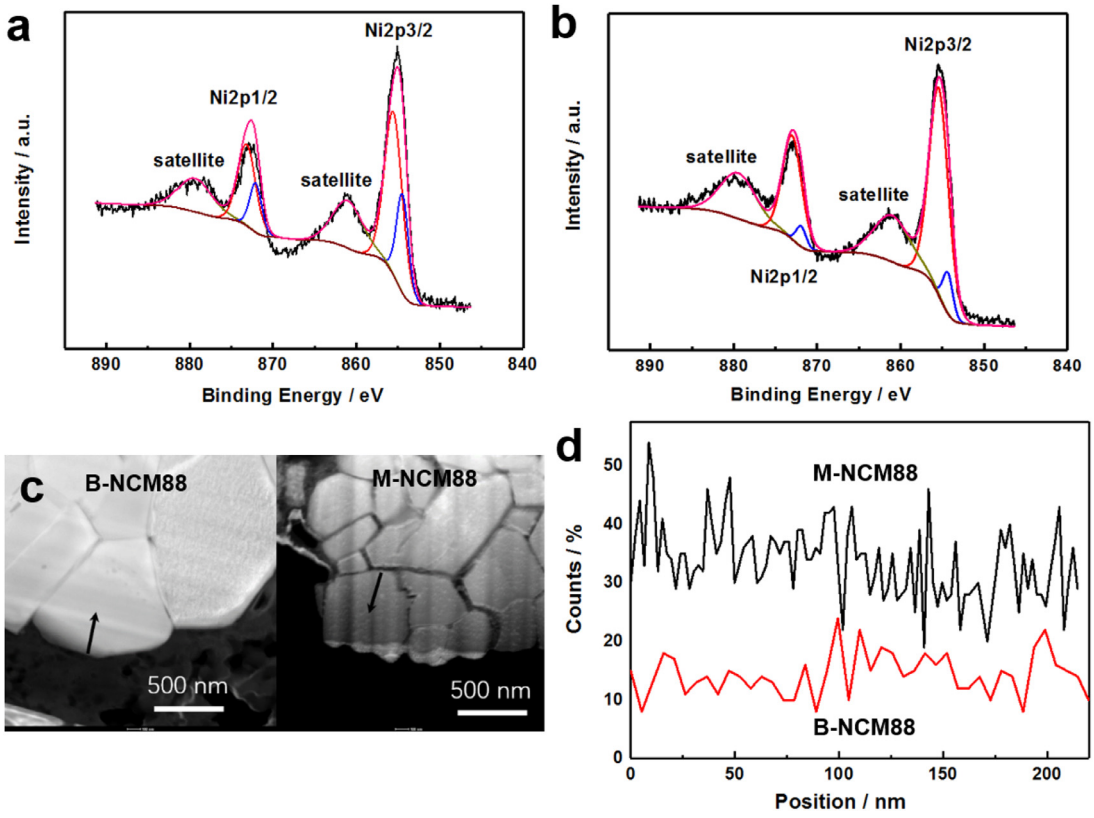

Fig. 5. XPS spectra of (a) M-NCM88, (b) B-NCM88; (c) the EDS Line scanning (arrow implies Scanning direction); (d) EDS spectra of oxygen content for two samples.

less stress-strain damage caused by charging/discharging. The Fig. 5f showed the whole corrosion and phase transition process of cathode during cycling. And the rock-salt phase nucleated and grew easily both at surface and bulk phase with oxygen defects. The intrinsic degradation exacerbates the formation of cycling-induced the cycling-induced degradation without protection, eventually leading to structure deterioration. Mn coating layer could reduce Ni valance state, improve structure stability and suppress the surface side reaction by inhabiting the formation of oxygen vacancy and cycling-induced defects.

The electrochemical performance of the B-NCM88 and M-NCM88 cathodes were examined using the LAND CT2001C. The 1st, 11th and 101th charge-discharge profiles of the B-NCM88 and M-NCM88 were presented in Fig. 7a, b in the voltage range of 2.8–4.25 V at 25 °C. The charge and discharge rate was 1 C. The 1st charge-discharge profile of the M-NCM88 showed relatively little capacity loss compared with B-NCM88 cathodes with Mn coated on it. The M-NCM88 sample delivered initial charge and discharge capacities of 198.9 and 182.0 mA h g^{-1} with a coulombic efficiency of 91.5%. And the B-NCM88 sample delivered initial charge and discharge capacities of 202.7 and 184.2 mA h g^{-1} with a coulombic efficiency of 90.8%. There was almost no gap between two samples at the first cycle. After 100 cycles, the capacity of M-NCM88 was 19.2 mA h g^{-1} higher than that of B-NCM88. The polarization of cathode was smaller for M-NCM88 in Fig. 7a. The cycling performance was shown in Fig. 7c. The M-NCM88 cathode presented an excellent long-term cycling performance, about 80.6% of the initial capacity after 200 cycles. In contrast, the capacity retention of B-NCM88 was only 47.2% in the voltage range of 2.8–4.25 V at 25 °C at 1 C. The 1st and 100th differential capacity curves of two samples were shown in Fig. 7d, e. The initial B-NCM88 and M-NCM88 cathodes, like Ni-rich cathodes, underwent a series of phase transitions during charging/discharging, as corroborated by the several oxidation peaks denoted in Fig. 7d: hexagonal to monoclinic (H1 to M), monoclinic to hexagonal (M to H2), and hexagonal to hexagonal (H2 to H3). In the final H2 to H3 phase transition process, subjected to a mechanically strained state, the Ni-rich cathode materials deteriorated its rechargeability. The intensity of the H2-to-H3 oxidation peak for the B-NCM88 cathode markedly dropped after 100 cycles, indicating poor irreversibility of the H2-to-H3 phase transition during cycling, which was related to the severe structural collapse caused by mechanical strain associated with cation mixing and oxygen loss. Other oxide phase transition potential shifted positively indicating a series lagged reactions. The lagged reactions meant irreversibility of cathode caused by phase transitions. Consistent with phase transitions in TEM images, the analysis via the electrochemistry verified the improvement of cycling and structure stability by the coating layer. Further electrochemical tests were further carried out by Electrochemical Impedance Spectroscopy (EIS) analysis. The smaller R_{ct} of M-NCM88 demonstrated the faster Li^+ ion migration rate and lower migration barrier at both the 1st cycle and the 11th cycle in Fig. 7f.

With the analysis of TEM images and electrochemical data of Ni-rich cathodes, the formation of NiO-like rock-salt is depended on oxygen loss and cation mixing, which is accelerated by lithium migration during the H2-to-H3 phase transition at high voltage state. The initial cathode material has certain defects. And the initial defects are deteriorated by lattice stress form charging/discharging, which is all the same to the surface and bulk phase. The oxygen of Ni-rich cathodes in bulk phase can be lost due to Jahn-Teller effect of transition metal unlike Ni-low cathodes such as NCM333 [27]. This process results in lattice stress damage and oxygen evolution, which explains the strain distribution by GPA. Furthermore, the oxygen defects accelerate the migration of Ni ion to Li site, which reduces the blocking effect of oxygen layers between Ni and Li layers. And it is regarded as the defect chain reaction, which evolves defects into phase transition. There is sufficient driving force to form oxygen defects in bulk phase for Ni-rich cathodes. It also explains why previous work holds that the rock-salt phase appears in the surface of cathodes in NCM333 or NCM523 [7,12,28]. Compared with B-NCM88,

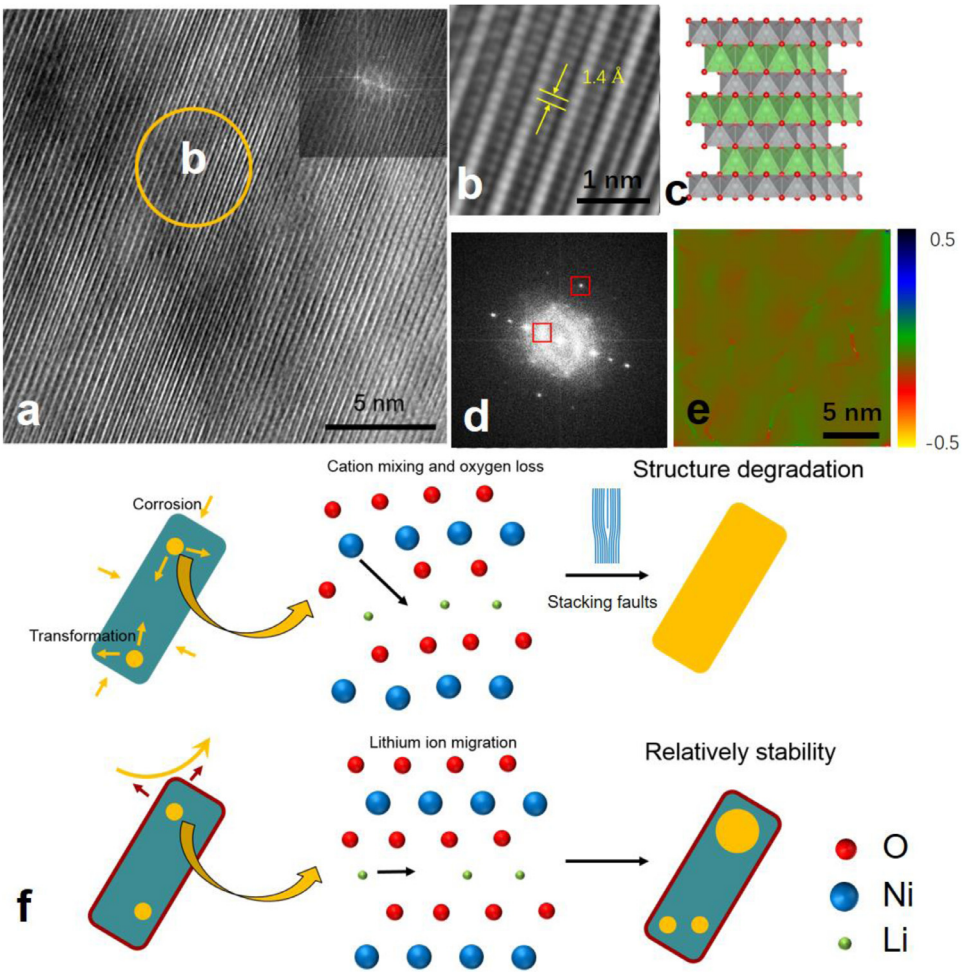

Fig. 6. (a-e) The TEM characterization of after 200 cycles: (a) bulk region of M-NCM88; (b) HRTEM images of corresponding region; (c) layered structure diagram; (d) the FFT filtered image for a; (e) the GPA in-plane strain (ε_{xx}) images for a. (f) the schematic of corrosion and phase transition process of cathode.

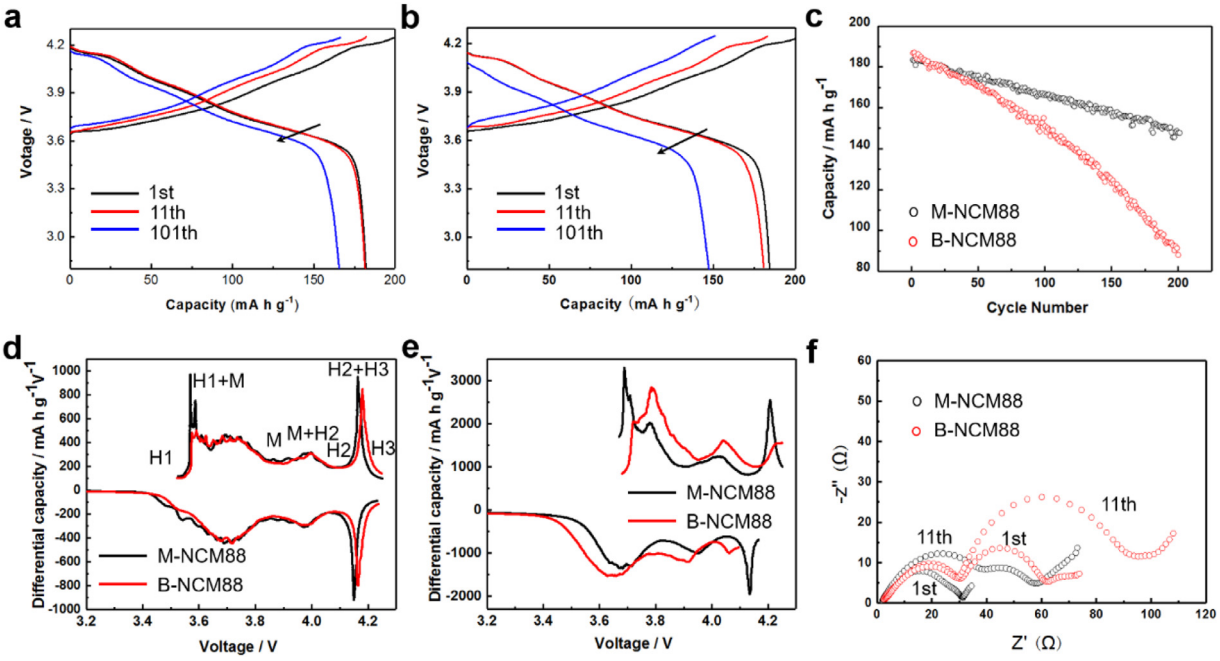

Fig. 7. The electrochemical performance of the B-NCM88 and M-NCM88 cathodes. Charge/discharge profiles of the (a) M-NCM88 and (b) B-NCM88; (c) cycling performance of two cathodes; (d-e) differential capacity curves of two cathodes; (f) EIS analysis.

the M-NCM88 shows a relatively stable performance due to the low electrochemical activity and stable structure of Mn coating layers.

3. Conclusion

This work demonstrates the novel understanding of potential evolution process for Ni-rich cathodes. The degradation in Ni-rich cathodes are split into the intrinsic degradation and cycling-induced degradation by the causes. The way of degradation is described as unlike any form of surface reaction previously reported. A mass of cycling-induced dislocation come to light from TEM. The intrinsic one contain a small amount of vacancy, dislocations and defects with lattice distortion. owing to the structural instability of Ni-rich cathodes, while the cycling-induced degradation are numerous accompanied by phase transition via a defect chain reaction (DCR). The intrinsic degradation amplifies the cycling-induced one, from surface to bulk. Defects are evolved into phase transition via DCR by introducing stress perpendicular to the Ni layers and causing the dislocation between layers with cation migration. Based on this phenomenon and the properties of Ni-rich cathode, a vacancy enhanced dislocation with lithium ion compensations mechanism is proposed evidenced by first principle calculation. To suppress the DCR, a Mn coating method was introduced to improve to electrochemical properties of the high nickel cathode $LiNi_{0.88}Co_{0.08}Mn_{0.04}O_2$ by inhabiting cycling-induced degradation via equilibrium valence state. The M-NCM88 cathode presented an excellent long-term cycling performance, about 80.6% of the initial capacity after 200 cycles. These interpretations enlighten materials design for layered cathode involving phase transition and stress damage in batteries.

4. Experimental methods

Synthesis of B-NCM88 and M-NCM88 Cathode Materials. The spherical precursor $Ni_{0.88}Co_{0.08}Mn_{0.04}(OH)_2$ was synthesized by a modified co-precipitation method [29]. Briefly, proper amounts of $NiSO_4$, $CoSO_4$ and $MnSO_4$ (cationic ratio of Ni: Co: Mn = 88:8:4) were added to a strongly stirred tank reactor under nitrogen atmosphere, forming a 2.0 mol L^{-1} solution. A 2.0 mol L^{-1} ammonia as a complexation agent and a 4.0 mol L^{-1} NaOH solution as precipitate agent were also pumped into the reactor at the same time. The obtained precursor was then dried at 120 °C for 4 h in the air. After drying, the precursor and $LiOH•H_2O$ were ball milled for 4 h to make uniform mixture. The Li/TM molar ratio of mixture was fixed at 1.05 [3,30]. The mixture was heated to 550 °C at a heating rate of 5 °C /min, then heated to 780 °C at a heating rate of 10 °C /min and finally calcined for 10 h in the O_2. The M-NCM88 sample was prepared in a 40 ml ethanol solution of 2 wt.% $(CH_3COO)_2Mn$. 10 g of the B-NCM88 cathode was added to the solution. The mixed solution was stirred at 60 °C until the solvent completely evaporated. The surface treated samples were then calcinated at 780 °C for 5 h in O_2.

Materials Characterization. The particle size distribution was measured on a laser diffraction instrument (Malvern Mastersizer 2000, Malvern, UK) with dynamic light scattering (DLS) methods. The thermal decomposition behaviors were investigated by thermal gravimetric analysis (TGA) at a heating rate of 3 oC/min. The sample structures were identified by using powder X-ray diffraction (XRD, Cu Kα radiation, Bruker D8 Advance). The morphology and element distribution were analyzed using a scanning electron microscope (SEM, Hitachi S-4800) equipped with an energy dispersive spectrometer (EDS, Horiba, EX-250) and a field-emission high resolution transmission electron microscope (HRTEM, JEM-2100F at 200 kV and Thermo Fisher Scientific (FEI) Tecnai F30 at 300 kV).

Electrochemical Tests. The working electrode was prepared by mixing active material (B-NCM88, 90 wt.%), carbon black conductive additive (Super P, 5 wt.%), and polyvinylidenefluoride binder (PVDF, 5 wt.%) dissolved in N-methylpyrrolidone (NMP). The slurry was then casted on aluminum foil and followed by drying at 120 °C for 24 h in vacuum oven. Electrolyte was a mixture of ethylene carbonate (EC), ethyl methyl carbonate (EMC), and dimethyl carbonate (DMC) containing lithium hexafluorophosphate (LiPF6) and Celgard 2400 film was used as separator. The cells were assembled in an argon-filled glove box with H_2O and O_2 concentrations below 0.05 ppm. All the electrochemical performances were performed on a LAND CT2001C (Wuhan, China) battery program-control test system between 2.8 and 4.25 V at different charge/discharge rate (1C = 190 m Ah g^{-1}) at 25 °C. Electrochemical impedance spectroscopy (EIS) was measured in the frequency range from 10^5 to 10^{-2} Hz with an amplitude of 5 mV (CHI660E, Shanghai, China). EIS measurements were performed at the charge state of 3.8 V after three cycles (0.1C/0.1C). Ni-rich cathode has a relatively low voltage platform. And the state of 3.8 V corresponds to about 60% state of charge.

DFT calculation. The DFT (density functional theory) calculation is within the generalized gradient approximation (GGA) from Pedrdw, Burke and Ernzerh (PBE) by VASP code [31]. The generalized gradient approximation + *U* formalism developed by Dudarev et al. [32] was employed for the 3d electrons of each transition metal cation species (the U values of Ni were 5.2 eV) [31,33]. As for $Li_{26}Ni_{27}O_{53}$ and its derivatives, a 3 × 3 × 2 k-point sampling was used, containing 26 Li atoms, 27 Ni atoms and 53 O atoms in a 3 × 3 × 1 super cell [34]. The plane-wave cutoff energy is 520 eV and an energy tolerance of 10^{-5} eV $atom^{-1}$ was used for the convergence. The maximum tolerance for force was 0.005 eV $Å^{-1}$ and the final morphology is determined by the model when the lowest total surface energy of the crystal is reached [22].

Declaration of Competing Interest

The authors declare that they have no known competing financial interests or personal relationships that could have appeared to influence the work reported in this paper.

CRediT authorship contribution statement

Chengkai Yang: Conceptualization, Methodology, Software, Formal analysis, Resources, Data curation, Writing - original draft, Writing - review & editing, Visualization, Supervision, Project administration. **Ruiwen Shao:** Methodology, Software, Data curation, Writing - review & editing, Visualization, Supervision. **Qian Wang:** Formal analysis, Resources, Data curation. **Tianyi Zhou:** Formal analysis. **Jing Lu:** Software. **Ning Jiang:** Software. **Peng Gao:** Methodology, Software, Formal analysis. **Wen Liu:** Resources. **Yan Yu:** Funding acquisition, Supervision. **Henghui Zhou:** Conceptualization, Resources, Funding acquisition, Supervision.

Data availability

Data will be made available on request.

Acknowledgement

The work is supported by the National Natural Science Foundation of China (21771018 and 21875004), and Natural Science Foundation of Beijing (Grant No. 2192018, No. 2192037). C.K. Y., R.W. S. and Q. W. contributed equally to this work. Technology Innovation Project of New Energy Vehicles Industry. PULEAD Technology Industry Co. Ltd is gratefully acknowledged for financial support. The DFT calculation was supported by High-performance Computing Platform of Peking University.

Supplementary materials

Supplementary material associated with this article can be found, in the online version, at doi:10.1016/j.ensm.2020.11.016.

References

[1] J. Zheng, M. Gu, J. Xiao, P. Zuo, C. Wang, J.-.G. Zhang, Nano Lett. 13 (2013) 3824.
[2] A. Boulineau, L. Simonin, J.-.F. Colin, C. Bourbon, S. Patoux, Nano Lett. 13 (2013) 3857 J. Betz, G. Bieker, P. Meister, T. Placke, M. Winter, R. Schmuch, Adv Energy Mater 2018, 9; S.-H. Jhi, J. Ihm, S. G. Louie, M. L. Cohen, Nature 1999, 399, 132; M. G. Kim, M. Jo, Y.-S. Hong, J. Cho, Chem. Commun. 2009, 218.
[3] M.M. Thackeray, C. Wolverton, E.D. Isaacs, Energy Environ. Sci. 5 (2012) 7854.
[4] F. Lin, I.M. Markus, D. Nordlund, T.-.C. Weng, M.D. Asta, H.L. Xin, M.M. Doeff, Nat. Commun (2014) 5.
[5] W. Liu, P. Oh, X. Liu, M.-.J. Lee, W. Cho, S. Chae, Y. Kim, J. Cho, Angew. Chem. 54 (2015) 4440.
[6] C. Yang, R. Shao, Y. Mi, L. Shen, B. Zhao, Q. wang, K. Wu, W. Lui, P. Gao, H. Zhou, J Power Sources 376 (2018) 200 ; C.-K. Yang, L.-Y. Qi, Z. Zuo, R.-N. Wang, M. Ye, J. Lu, H.-H. Zhou, J Power Sources 2016, 331, 487.
[7] S.-.K. Jung, H. Gwon, J. Hong, K.-.Y. Park, D.-.H. Seo, H. Kim, J. Hyun, W. Yang, K. Kang, Adv. Energy Mater. (2014) 4.
[8] K.-.J. Park, H.-.G. Jung, L.-Y. Kuo, P. Kaghazchi, C.S. Yoon, Y.-K. Sun, Adv. Energy Mater. (8) (2018).
[9] H.-.H. Ryu, K.-.J. Park, C.S. Yoon, Y.-.K. Sun, Chem. Mater. 30 (2018) 1155.
[10] S. Liu, Z. Dang, D. Liu, C. Zhang, T. Huang, A. Yu, J. Power Sources 396 (2018) 288 N. Wu, Y. Zhang, Y. Guo, S. Liu, H. Liu, H. Wu, ACS Appl. Mater. Interfaces 2016, 8, 2723.
[11] H. Yu, Y. Qian, M. Otani, D. Tang, S. Guo, Y. Zhu, H. Zhou, Energy Environ. Sci. 7 (2014) 1068 ; Y. Cho, P. Oh, J. Cho, Nano Lett. 2013, 13, 1145.
[12] H. Zhang, F. Omenya, M.S. Whittingham, C. Wang, G. Zhou, ACS Energy Lett. 2 (2017) 2598.
[13] P. Yan, J. Zheng, J.G. Zhang, C. Wang, Nano Lett. 17 (2017) 3946.
[14] D. Liu, S. Liu, C. Zhang, L. You, T. Huang, A. Yu, ACS Sustain Chem Eng 7 (2019) 10661 H. Kim, S. Lee, H. Cho, J. Kim, J. Lee, S. Park, S. H. Joo, S. H. Kim, Y. G. Cho, H. K. Song, S. K. Kwak, J. Cho, Adv Mater 2016, 28, 4705.
[15] C. Xu, K. Märker, J. Lee, A. Mahadevegowda, P.J. Reeves, S.J. Day, M.F. Groh, S.P. Emge, C. Ducati, B.L. Mehdi, C.C. Tang, C.P. Grey, Nat. Mater. (2020).
[16] W. Lee, S. Muhammad, T. Kim, H. Kim, E. Lee, M. Jeong, S. Son, J.-.H. Ryou, W.-.S. Yoon, Adv. Energy Mater. 8 (2018) H. Chen, J. A. Dawson, J. H. Harding, J Mater Chem A 2014, 2; K.-J. Park, H.-G. Jung, L.-Y. Kuo, P. Kaghazchi, C. S. Yoon, Y.-K. Sun, Adv Energy Mater 2018, 8, 1801202.
[17] S. Li, Z. Yao, J. Zheng, M. Fu, J. Cen, S. Hwang, H. Jin, A. Orlov, L. Gu, S. Wang, Z. Chen, D. Su, Angew. Chem. Int. Ed. Engl. (2020).
[18] Y. Kim, D. Kim, S. Kang, Chem. Mater. 23 (2011) 5388 Y. Koyama, H. Arai, I. Tanaka, Y. Uchimoto, Z. Ogumi, Chem Mater. 2012, 24, 3886; E.-J. Lee, Z. Chen, H.-J. Noh, S. C. Nam, S. Kang, D. H. Kim, K. Amine, Y.-K. Sun, Nano Lett. 2014, 14, 4873.
[19] T. Maiyalagan, K.A. Jarvis, S. Therese, P.J. Ferreira, A. Manthiram, Nat. Commun. (2014) 5.
[20] F. Lin, I.M. Markus, D. Nordlund, T.C. Weng, M.D. Asta, H.L. Xin, M.M. Doeff, Nat. Commun. 5 (2014) 3529 P. Yan, J. Zheng, M. Gu, J. Xiao, J. G. Zhang, C. M. Wang, Nat Commun 2017, 8, 14101.
[21] Y. Kim, J. Mol. Struct. 1099 (2015) 317.
[22] Y. Kim, D. Kim, S. Kang, Chem. Mater. 23 (2011) 5388.
[23] P. Yan, J. Zheng, J. Liu, B. Wang, X. Cheng, Y. Zhang, X. Sun, C. Wang, J.-.G. Zhang, Nat. Energy 3 (2018) 600.
[24] L.W. Peng Gao, Y. Zhang, Y. Huang, K. Liu, ACS Nano 9 (2015) 11296.
[25] P. Gao, Y.Y. Zhang, L.P. Wang, S.L. Chen, Y. Huang, X.M. Ma, K.H. Liu, D.P. Yu, Nano Energy 32 (2017) 302 ; H.-C. Y. Wei Zhang, Lijun Wu, Hao Liu, Aziz Abdellahi, Bao Qiu, Jianming Bai, Bernardo Orvananos, Fiona C. Strobridge, Xufeng Zhou, Zhaoping Liu, Gerbrand Ceder, Yimei Zhu, Katsuyo Thornton, Clare P. Grey, Feng Wang, Sci. Adv. 2018, 4.
[26] D.-.S. Ko, J.-.H. Park, B.Y. Yu, D. Ahn, K. Kim, H.N. Han, W.S. Jeon, C. Jung, A. Manthiram, Adv. Energy Mater. (2020) 2001035 n/a.
[27] R. Stoyanova, E. Zhecheva, R. Alcántara, J.L. Tirado, J. Mater. Chem. 16 (2006) 359.
[28] X. Li, H. Peng, M.-.S. Wang, X. Zhao, P.-.X. Huang, W. Yang, J. Xu, Z.-.Q. Wang, M.-.Z. Qu, Z.-.L. Yu, Chem. Electro. Chem. 3 (2016) 130.
[29] H. Kim, S. Lee, H. Cho, J. Kim, J. Lee, S. Park, S.H. Joo, S.H. Kim, Y.G. Cho, H.K. Song, S.K. Kwak, J. Cho, Adv. Mater. 28 (2016) 4705 ; T.-P. Gao, K. W. Wong, K. Y. Fung, W. Zhang, K. M. Ng, Electrochim Acta. 2018, 288, 153.
[30] M.M. Thackeray, S.-.H. Kang, C.S. Johnson, J.T. Vaughey, R. Benedek, S.A. Hackney, J. Mater. Chem. 17 (2007) 3112.
[31] D. Vanderbilt, Phys. Rev. B 41 (1990) 7892.
[32] S.L. Dudarev, G.A. Botton, S.Y. Savrasov, C.J. Humphreys, A.P. Sutton, Phys. Rev. B 57 (1998) 1505.
[33] C. Berger, Z. Song, X. Li, X. Wu, N. Brown, C. Naud, D. Mayou, T. Li, J. Hass, A.N. Marchenkov, E.H. Conrad, P.N. First, W.A. de Heer, Science 312 (2006) 1191 ; F. Zhou, M. Cococcioni, C. A. Marianetti, D. Morgan, G. Ceder, Phys Rev B 2004, 70, 235121.
[34] Y. Kim, H. Lee, S. Kang, J. Mater. Chem. 22 (2012) 12874 ; Y. Koyama, H. Arai, I. Tanaka, Y. Uchimoto, Z. Ogumi, Chem. Mater. 2012, 24, 3886.